Available online at www.sciencedirect.com
ScienceDirect
Journal of Sound and Vibration 322 (2009) 78–97
JOURNAL OF SOUND AND VIBRATION
www.elsevier.com/locate/jsvi

Tuning fork microgyrometers: Narrow gap vs. wide gap design

L. Soria*, E. Pierro, G. Carbone, T. Contursi

Politecnico di Bari, Dipartimento di Ingegneria Meccanica e Gestionale, V.le Japigia, 182 - 70126 Bari, Italy

Received 4 August 2007; received in revised form 20 October 2008; accepted 28 October 2008
Handling Editor: C.L. Morfey
Available online 15 January 2009

Abstract

We analyse the performances of two different configurations of a tuning fork microgyrometer, the so called 'wide gap' design and 'narrow gap' design. In the former case the air gap between the vibrating forks and the walls of the surrounding frame is so large that the air flow around each fork is not influenced by the presence of the frame itself. This geometrical configuration results in a very low air damping, and, hence, allows the instrument to operate at atmospheric pressure. In the case of 'narrow gap' design the distance between the forks and the frame walls is instead very small. As a consequence, the instrument needs to operate under very low pressure conditions, since, at higher pressures, the presence of a thin layer of air would increase the air damping to very large values, and would not allow the correct operation of the instrument. Although the requirement of low pressure conditions represents a drawback of the narrow gap solution, we show that this instrument configuration, when compared to the wide gap design, allows to achieve a significantly smaller dynamic error and a significantly wider range of linearity. Indeed the thickness of the air gap represents an additional parameter that can be adjusted by the designer to optimise the performances of the instrument. An accurate analytical model of the sensor is presented in the paper, which constitutes a helpful designing tool for this kind of device. In particular we focus the attention on the two tines of the drive mode, which are indeed the structural components that more than others influence the instrument performances. We show that the optimal design of these fundamental elements can be obtained by neglecting the interaction with the remaining part of the sensor structure, and show how to design the instrument to minimise the amplitude error. The influence of air damping, structural damping and geometry on the system response in terms of bandwidth and dynamic error is also investigated.

1. Introduction

A microgyroscope is an angular rate sensor that uses the effect of the Coriolis force acting on a reciprocating proof mass to measure the angular velocity of the device. There are two kinds of motions of the mass, the input or drive motion and the output or sense motion. Recently a great number of microgyroscopes has been developed with different design. There are oscillators that realise the two motions in two orthogonal planes [1–5] or in the same plane [6–8] and devices that use a silicon cantilever beam [9–13] or a ring-type structure [14]. Furthermore they can use many principles of actuation and detection, such as piezoelectric [15],

*Corresponding author. Tel.: +39 080 596 2813; fax: +39 080 596 2777.
E-mail address: soria@poliba.it (L. Soria).

0022-460X/$ - see front matter © 2008 Elsevier Ltd. All rights reserved.
doi:10.1016/j.jsv.2008.10.034

optical [12], electrostatic [2] and piezoresistive [10]. For all these devices the research effort has been focusing on the improvement and the optimisation of the output signal quality, measured by the so called 'sensitivity' (that is the ratio between the amplitude of the output motion and the angular velocity to be measured), and by the resolution of the instrument. The methods more often employed to improve the instrument performances are (i) the matching of the drive and sense resonant frequencies [6,7], (ii) the reduction of air pressure, i.e. of the air damping [2,5,16], (iii) the designing of symmetrical structures [6,7] and (iv) the adoption of independent beams for the two modes [1]. However the enormous demand of such devices from automotive, aeronautics, mobile phone and robotics market, has led to a fast development of simple models to describe the dynamic behaviour of these sensors [1,8,10,12–14]. Two degrees of freedom lumped models are often utilised for the design of these systems. However, the simplicity of such models limits the possibility of optimising the design of the instrument to get better performances.

With the purpose of providing a more advanced tool to designers, in this paper we have developed an accurate, mass-distributed, analytical model to describe the dynamics of a double tuning fork microgyroscope. Our interest is, indeed, directed to the determination of the main functional parameters which the instrument operation depends on and to the optimisation of the instrument performances by choosing the appropriate values of those parameters (physical or geometrical) which the designer is free to modify.

In the most common design these devices operate at atmospheric pressure with an air gap large enough to allow to neglect the presence of the substrate on the evaluation of the drag force acting on the structural elements. The air damping, being related to the fluid viscosity, depends on the environmental pressure. However, in this paper, we have also considered a different possible design characterised by the presence of a really narrow air gap between the structure and the substrate. In this case the air damping is strongly affected by the thickness of the gap, and if the air pressure were kept at the atmospheric value, this would lead to very high damping factors, and, in turn, would prevent the correct operation of the instrument. For this reason, the narrow gap configuration requires the device be vacuum-encapsulated.

We analyse and compare the dynamic responses of both the instrument designs (wide gap and narrow gap) by focusing the attention on the drive mode structural components, which significantly influence the performance of the whole instrument. In particular our analysis is concerned with the drive beams, that undergo two different motions: one is parallel to the rotating substrate, and will be referred to as the drive motion, the other one occurs along the perpendicular direction (the sense motion). A continuum description of the drive beam has been developed for both the considered sensor configurations and the resulting mathematical equations have been analytically solved for both the cases examined. The model takes into account the influence of different damping mechanisms: the air damping and the structural damping (thermoelastic damping is shown to be negligible). Regarding the air damping mechanism it is worth to observe that in the narrow gap design the lateral damping affecting the drive motion is usually much smaller than the squeeze damping which, instead, affects the sense motion, and this in turn produces a very different response of the system if compared to the wide gap configuration. In both the cases the device sensitivity improves when the beam is designed with a square cross section; however, the narrow gap design has the advantage of being much less affected by small manufacturing errors. Indeed, such errors may led to beam aspect ratios slightly different from 1, which in the case of the wide gap configuration, we show to cause a tremendous response reduction. We also show that, in the narrow gap configuration, the presence of the air layer between the forks and the substrate can be regarded as an additional design parameter, that, if properly chosen, may lead to a reduction of the dynamic error of the device and can be utilised by the designer to modify the instrument range of linearity.

2. Dynamic model

The vibrating microgyroscope has a double tuning fork quartz structure, the 'drive tines' and the 'sense tines'. Both of them are supported by a frame connected by two flexures to a central mounting post (attached to the rotating substrate) as shown in Fig. 1. The two drive tines are piezoelectrically actuated and they oscillate along the x-axis. When the substrate is rotating about the y-axis, the Coriolis force produces an alternating out of plane bending of the drive tines, and in turn a reaction torque. This torque puts in rotation

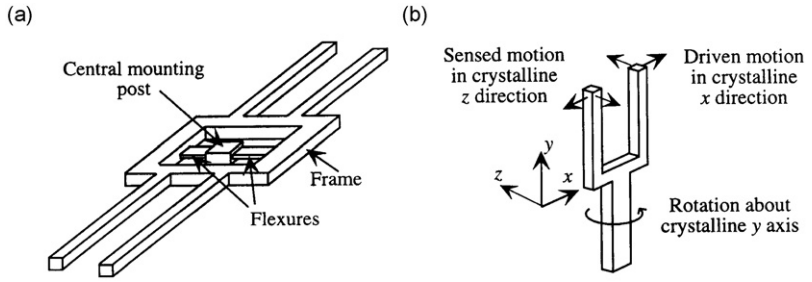

Fig. 1. The scheme of the quartz angular rate sensor (a) and the tuning fork of the drive mode (b).

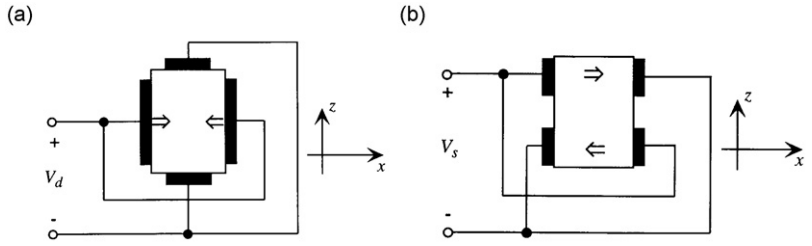

Fig. 2. The electrode configuration for the drive mode (a) and for the sense mode (b).

the frame and, as a consequence, generates the out of plane motion of the sense tines, thus producing an output piezoelectric signal proportional to the angular velocity to be measured.

In this work, two sources of energy dissipation have been considered affecting the behaviour of the device, the air damping and the structural damping. The thermoelastic damping, as shown in Ref. [17], can instead be reduced to zero with an optimal choice of the beam geometrical dimensions and for this reason it has not been included in the analysis. As already stated above, we analyse two different configurations of the microgyrometer, which we refer to as the 'wide gap' and 'narrow gap' designs. From the point of view of damping factors, the main differences between the two configurations are that in the case of the narrow gap design the lateral damping is much smaller than the squeeze damping, and that the air pressure, which the instruments operates at, is very small. In such situations of very low pressure conditions the structural damping can be comparable to the air damping and has to be properly taken into account. When, instead, the instrument is supposed to work at atmospheric pressure the structural damping can be neglected [1,8,10,12–14].

Both the actuation and the sensing mechanisms of the device utilise the piezoelectric effect, that couples the strain field of a structure with the electric field through the well-known constitutive equation of electroelasticity. The configuration of the electrodes on the surface of the quartz tines is different for the two modes as shown in Fig. 2. The piezoelectrically actuated bending of the drive tines is obtained in a plane parallel to the substrate, while the bending of the sense tines, which produces the electric field to be detected, occurs perpendicularly to the substrate. The externally applied electrical potential is time dependent, of the form $V(t) = \mathscr{V} \sin(\omega t)$, where the (radian) excitation frequency ω is generally chosen equal to the first bending natural frequency of the drive tines in the xy-plane.

The two drive tines, as well as the sense beams, are supposed to be symmetric with respect to the yz-plane. As a consequence, the dynamic behaviour of only one drive tine needs to be investigated. The drive tine is described as the beam of length L, shown in Fig. 3. The vertical displacement of the beam support, which is related to the torsional rotation of the frame, is shown to be negligible, and does not need to be taken into account. Indeed, the corresponding mechanical impedance is very high as a consequence of the relatively big mass of the frame, the small stiffness of the flexures and the high value of the excitation frequency. This conclusion is in agreement with Ref. [15] where it is shown that the amplitude of the support motion is several orders of magnitude smaller than the free end motion amplitude of the tines and a rough estimate gives 10^{-11} m for the amplitude of the support and 10^{-8} m for the amplitude of the free end. For this reason, the

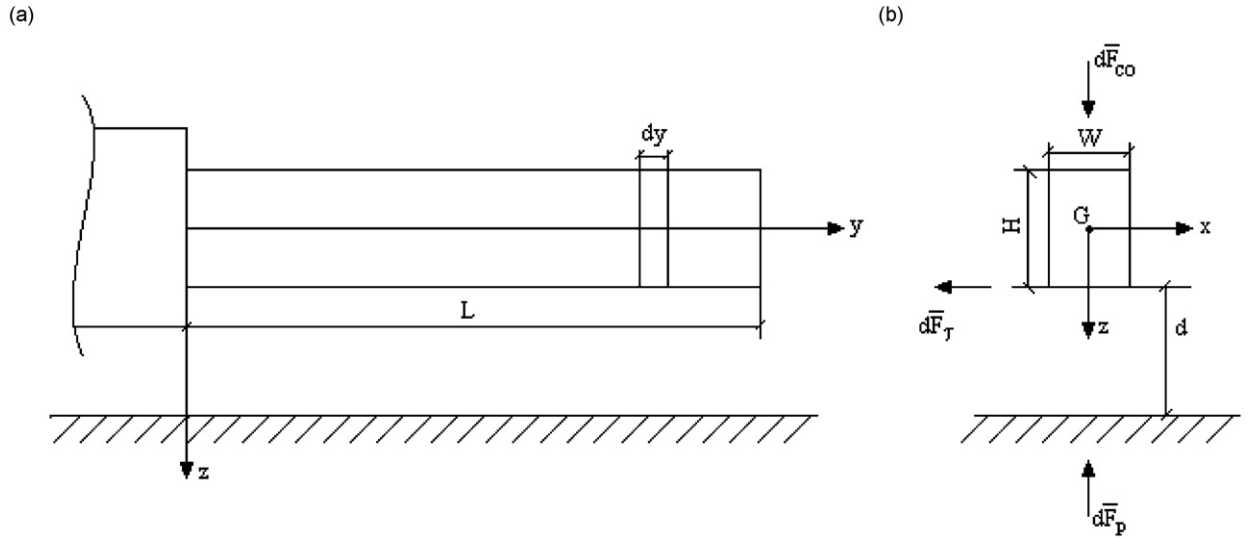

Fig. 3. The scheme of one of the two drive tines (a) and the forces acting on the generic section of the beam when the system is rotating (b). In $y = 0$, the mechanical impedance is Z_0.

functional design of the beam can be carried out, at a first approximation, by neglecting the interaction with the frame and by modelling each drive tine as it were actually a cantilever. This allows to write the equilibrium equations of the beam, in the xy- and yz-planes, as

$$EJ_z\frac{\partial^4 u_x}{\partial y^4} + \rho_q A\frac{\partial^2 u_x}{\partial t^2} = q_x \tag{1}$$

$$EJ_x\frac{\partial^4 u_z}{\partial y^4} + \rho_q A\frac{\partial^2 u_z}{\partial t^2} = q_z \tag{2}$$

where $E = 1/S_{yy}$ (S_{IJ} being the generic compliance coefficient, as explained ahead) and ρ_q are the Young modulus and the density of quartz, respectively, J_z and J_x are the inertia moments of the beam with respect to neutral axes, in the xy- and yz-planes, respectively, and $A = WH$ is the beam section area (Fig. 3b).

When the device is rotating, two types of mechanical forces act on the generic beam element of length $\mathrm{d}y$ and mass $\mathrm{d}m = \rho_q A\,\mathrm{d}y$. These forces are the apparent forces and the damping forces due to the presence of the air. The centrifugal force and the Euler force are both negligible since they are proportional to Ω^2 and $\dot{\Omega}$, respectively, where Ω is the rotation rate of the substrate which the beam is connected to. Hence, only the Coriolis force has to be taken into account, that gives rise to the two components per unit length $q_{1x} = -2\rho_q A\Omega\dot{u}_z$ and $q_{1z} = 2\rho_q A\Omega\dot{u}_x$.

The contribution of structural damping is taken into account in the usual way, by simply replacing in the equations of motion the real elasticity modulus E with the complex one $E' = E(1 + i\eta_s)$, where η_s is the structural damping coefficient (for quartz $\eta_s \approx 5 \times 10^{-6}$ [18]).

2.1. Wide gap design

In the case of the wide gap design, the device operates at atmospheric pressure. In order to describe the effects of the fluid flow around the beam, we use the string-of-beads model, which is often utilised for micro-machined cantilevers and resonators [19–22]. The basic idea is to model the vibrating beam as constituted of a certain number of spheres of diameter $2r$. The diameter $2r$ of the spheres is equal to the length of that edge of the beam cross section which is perpendicular to the beam motion direction. In our case $2r = H$ in the drive motion case and $2r = W$ in the sense motion case. The drag $F_{v,i}$ acting on the i-th sphere can be evaluated by recalling the Landau solution of damping of a harmonically vibrating sphere immersed in a viscous fluid [23].

The solution reads

$$F_{v,i} = -(6\pi\eta r + 3\pi r^2\sqrt{2\rho_a\eta\omega})v_i \tag{3}$$

where η and ρ_a are air viscosity and density, ω is the oscillation frequency of the element, r is the sphere radius and v_i is the sphere velocity. This approximation is in good agreement with experimental data as shown in Refs. [19,20]. As a consequence, the damping forces per unit length in the two planes can be simply written as

$$q_{2x} = \frac{1}{H}F_{v,i}\bigg|_{2r=H} = -\left(3\pi\eta + \frac{3}{4}\pi H\sqrt{2\rho_a\eta\omega}\right)\dot{u}_x \tag{4}$$

$$q_{2z} = \frac{1}{W}F_{v,i}\bigg|_{2r=W} = -\left(3\pi\eta + \frac{3}{4}\pi W\sqrt{2\rho_a\eta\omega}\right)\dot{u}_z \tag{5}$$

2.2. Narrow gap design

In the case of narrow gap design, high sensitivity of the instrument can be achieved only if the microgyroscope operates at low pressures ($\approx 1500-2000$ Pa), which in turn makes it necessary to take into account the effect of rarefaction on air viscosity. This is needed since the mean free path $\lambda = (\eta/p)\sqrt{\pi RT/2}$ of the molecules (p, T, R and η are pressure, temperature, elastic constant and viscosity of gas, respectively) rapidly grows as the pressure is decreased, and when λ becomes comparable to the air gap dimension d, the fluid cannot be longer treated as a continuum body and a correction for the fluid viscosity has to be employed. This is indeed our case since the Knudsen number $K_n = \lambda/d$ is relatively high (≈ 5), so that it is necessary to calculate the effective air viscosity by means of the formula [24,25]

$$\eta_{\text{eff}} = \frac{\eta}{1 + 9.638K_n^{1.159}} \tag{6}$$

The value utilised in the paper is $\eta_{\text{eff}} = 3.3\times10^{-7}\,\text{N s m}^{-2}$.

To describe the lateral and squeeze damping due to air–beam interaction we have employed the Reynolds equation [26], that in the xz-plane takes the form

$$\frac{\partial}{\partial x}\left(\frac{\rho h^3}{12\eta_{\text{eff}}}\frac{\partial p}{\partial x}\right) = \frac{\partial(\rho h)}{\partial t} \tag{7}$$

where ρ and p are the density and the pressure of the air, respectively. Assuming an incompressible fluid film, the following air pressure distribution in the xz-plane can be obtained by integrating Eq. (7) with boundary conditions $p(-W/2,t) = p(W/2,t) = 0$

$$p = \frac{6\eta_{\text{eff}}\dot{h}}{h^3}\left(x^2 - \frac{W^2}{4}\right) = -\frac{6\eta_{\text{eff}}\dot{u}_z}{(d-u_z)^3}\left(x^2 - \frac{W^2}{4}\right) \tag{8}$$

where $h = d - u_z(y,t)$, as shown in Fig. 3b, is the difference between the distance d between the beam and the substrate in static conditions and the beam vertical displacement $u_z(y,t)$. In what follows we will simply use $h \approx d$, because typically the ratio between $|u_z|$ and d is order of 10^{-2} [24]. Since, indeed, the maximum $|u_z|$-values found in current applications are 10–60 nm and since d can be $1-5\,\mu$m, the approximation is certainly justified.

When the beam oscillates in a plane parallel to the substrate, a lateral viscous damping arises, due to the shear stress [26], given by

$$\tau_{zx,\text{fl}} = \eta_{\text{eff}}\frac{\partial u_{x,\text{fl}}}{\partial z}\bigg|_{z=H/2} = -\frac{h}{2}\frac{\partial p}{\partial x} - \frac{\eta_{\text{eff}}}{h}\dot{u}_x \approx \frac{6\eta_{\text{eff}}\dot{u}_z}{d^2}x - \frac{\eta_{\text{eff}}}{d}\dot{u}_x \tag{9}$$

where $u_{x,\text{fl}}$ is the fluid velocity component along the x-axis. This allows us to calculate the lateral damping force per unit length acting on the beam as

$$q_{2x} = -\frac{\eta_{\text{eff}}W}{d}\dot{u}_x \tag{10}$$

For the sense motion, the squeeze damping force per unit length is instead

$$q_{2z} = -\frac{\eta_{\text{eff}} W^3}{d^3}\dot{u}_z \tag{11}$$

2.3. Piezoelectric actuation

Let us recall the constitutive equation of electro-elasticity, written in the form

$$\varepsilon_I = \sum_J S_{IJ}\sigma_J + \sum_j E_j d_{jI} \tag{12}$$

where ε_I is the strain, S_{IJ} are the compliance coefficients, σ_J is the stress, E_j is the electric field and d_{jI} are the piezoelectric strain coefficients.

To determine the equivalent stress caused by the electric field, we have firstly considered the simple case of the electrode configuration producing in the beam cross section an homogeneous electric field. In Ref. [27] it has been shown that the equivalent mechanical stress, along the y-axis, is in this case:

$$\bar{\sigma}_y = -\frac{d_{xy}}{S_{yy}}E_x \tag{13}$$

where the ratio d_{xy}/S_{yy} is the 'effective stress coefficient'.

Secondly, since the electric field due to the external applied potential is available in literature in the case of the drive mode configuration of electrodes represented in Fig. 2a [15], by using Eq. (13) we have calculated the equivalent mechanical bending moment acting on the beam cross section as

$$M_{\text{piezo}}(t) = \int_{-H/2}^{H/2}\int_{-W/2}^{W/2} \bar{\sigma}_y x \,\mathrm{d}x\,\mathrm{d}z = \mathrm{Im}(\bar{M}_{\text{piezo}}\,\mathrm{e}^{\mathrm{i}\omega t}) \tag{14}$$

and, therefore, defined the amplitude of the piezoelectric actuation as $\mathscr{A}_{\text{piezo}} = -\bar{M}_{\text{piezo}}/(EJ_z)$.

2.4. Model equations

The final form of the equations of motion are thus given by

$$\rho_q A\frac{\partial^2 u_x}{\partial t^2} + \beta_x\frac{\partial u_x}{\partial t} + 2\rho_q A\Omega\frac{\partial u_z}{\partial t} + E'J_z\frac{\partial^4 u_x}{\partial y^4} = 0 \tag{15}$$

$$\rho_q A\frac{\partial^2 u_z}{\partial t^2} - 2\rho_q A\Omega\frac{\partial u_x}{\partial t} + \beta_z\frac{\partial u_z}{\partial t} + E'J_x\frac{\partial^4 u_z}{\partial y^4} = 0 \tag{16}$$

where in the wide gap case one has $\beta_x = 3\pi\eta + (3/4)\pi H\sqrt{2\rho_a\eta\omega}$ and $\beta_z = 3\pi\eta + (3/4)\pi W\sqrt{2\rho_a\eta\omega}$, whereas in the narrow gap case $\beta_x = \eta_{\text{eff}}W/d$ and $\beta_z = \eta_{\text{eff}}W^3/d^3$. The general steady-state solution of the homogeneous system of partial differential equations (15, 16) has the form

$$u_x(y,t) = U_x(y)\,\mathrm{e}^{\mathrm{i}\omega t} \tag{17}$$

$$u_z(y,t) = U_z(y)\,\mathrm{e}^{\mathrm{i}\omega t} \tag{18}$$

and the needed boundary conditions are:

$$u_x(0,t) = 0, \quad \frac{\partial u_x}{\partial y}(0,t) = 0, \quad \frac{\partial^2 u_x}{\partial y^2}(L,t) = \mathscr{A}_{\text{piezo}}\,\mathrm{e}^{\mathrm{i}\omega t}, \quad \frac{\partial^3 u_x}{\partial y^3}(L,t) = 0 \tag{19}$$

$$\frac{-EJ_x\partial^3 u_z(0,t)/\partial y^3}{\partial u_z(0,t)/\partial t} = Z_0, \quad \frac{\partial u_z}{\partial y}(0,t) = 0, \quad \frac{\partial^2 u_z}{\partial y^2}(L,t) = 0, \quad \frac{\partial^3 u_z}{\partial y^3}(L,t) = 0 \tag{20}$$

The third of conditions (19) is related to the piezoelectric actuation as discussed in Section 2.3, while the complex quantity Z_0 in the first of conditions (20) represents the mechanical impedance of the section where the beam is connected to the frame ($y = 0$). This quantity is a function of the excitation frequency ω, besides of the geometry and the mass, stiffness and damping distributions of the remaining part of the whole device. As Z_0 approaches infinity, the first of conditions (20) becomes rigid, i.e. $u_z(0, t) = 0$. We utilise this formulation of the boundary condition in the model since, as stated above, the motion of the mass of the frame is negligible in comparison to the motion of the free end of the beam.

3. Dimensionless formulation

We can rephrase the model in a dimensionless form considering as fundamental quantities the beam length L, the excitation frequency ω and the quartz density ρ_q. After simple calculations one gets

$$\frac{\partial^2 \tilde{u}_x}{\partial \tau^2} + \zeta_x \frac{\Gamma}{\mu} \frac{1}{\rho_1 k_1} \frac{\partial \tilde{u}_x}{\partial \tau} + 2\frac{\Omega \partial \tilde{u}_z}{\omega \partial \tau} + \frac{1 + i\eta_s}{\rho_1^2 k_1^2} \frac{\partial^4 \tilde{u}_x}{\partial \tilde{y}^4} = 0 \tag{21}$$

$$\frac{\partial^2 \tilde{u}_z}{\partial \tau^2} + \zeta_z \frac{\Gamma}{\mu} \frac{1}{\rho_1 k_1} \frac{\partial \tilde{u}_z}{\partial \tau} - 2\frac{\Omega \partial \tilde{u}_x}{\omega \partial \tau} + \frac{1 + i\eta_s}{\rho_1^2 k_1^2} \mu^2 \frac{\partial^4 \tilde{u}_z}{\partial \tilde{y}^4} = 0 \tag{22}$$

where $\tilde{u}_x = u_x/L$, $\tilde{u}_z = u_z/L$, $\tau = \omega t$, $\tilde{y} = y/L$, $\Gamma = \mu \eta_{\text{eff}} L^2/(\rho_q A c r_z)$, $\mu = \omega_{n,1}^{(z)}/\omega_{n,1}^{(x)} = H/W$, $\rho_1 = \omega/\omega_{n,1}^{(x)}$. The first natural frequency $\omega_{n,1}^{(x)}$, in the xy-plane is

$$\omega_{n,1}^{(x)} = \sqrt{\left(\frac{k_1}{L^2}\right)^2 \frac{EJ_z}{\rho_q A}} = c r_z \frac{k_1}{L^2} \tag{23}$$

with $k_1 = (1.875104)^2$ in the cantilever beam case (Euler–Bernoulli theory), $c^2 = E/\rho_q$, $r_z^2 = J_z/A$. In particular, in the wide gap design case one has the damping coefficients $\zeta_x = 3\pi\chi[1 + (\sqrt{2}/4)\mu(\sqrt{\rho_a/\rho_q})/(\sqrt{\Gamma\chi/\rho_1 k_1})]$ and $\zeta_z = 3\pi\chi[1 + (\sqrt{2}/4)(\sqrt{\rho_a/\rho_q})/(\sqrt{\Gamma\chi/\rho_1 k_1})]$, with $\chi = \eta/\eta_{\text{eff}}$, while in the narrow gap design case they are $\zeta_x = \zeta$ and $\zeta_z = \zeta^3$, with $\zeta = W/d$. Observe that the quantity ρ_1 is always equal to 1, during operation, in order to get the amplitude of the drive motion highly magnified. The boundary conditions (19) and (20) can be rephrased in dimensionless terms as

$$\tilde{u}_x(0, \tau) = 0, \quad \frac{\partial \tilde{u}_x}{\partial \tilde{y}}(0, \tau) = 0, \quad \frac{\partial^2 \tilde{u}_x}{\partial \tilde{y}^2}(1, \tau) = \mathscr{A}_{\text{piezo}} L e^{i\tau}, \quad \frac{\partial^3 \tilde{u}_x}{\partial \tilde{y}^3}(1, \tau) = 0 \tag{24}$$

$$\tilde{u}_z(0, \tau) = 0, \quad \frac{\partial \tilde{u}_z}{\partial \tilde{y}}(0, \tau) = 0, \quad \frac{\partial^2 \tilde{u}_z}{\partial \tilde{y}^2}(1, \tau) = 0, \quad \frac{\partial^3 \tilde{u}_z}{\partial \tilde{y}^3}(1, \tau) = 0 \tag{25}$$

The analytical solution of the homogeneous partial differential equations (21, 22) is reported in Appendix B. It is worth to notice that the non-dimensional parameter Γ can be written as

$$\Gamma = \mu \frac{\eta_{\text{eff}} L^2}{\rho_q A c r_z} = \sqrt{12} \frac{\eta_{\text{eff}}}{\rho_q c W} \left(\frac{L}{W}\right)^2 \tag{26}$$

and hence it can be easily considered only depending on viscosity if the other quantities are kept constant. For this reason, in the following considerations, changes of the beam cross section aspect ratio μ will be obtained by varying H values only, thus not affecting the value of Γ.

4. Results

We will focus on the dynamics of the free end of the beam ($\tilde{y} = 1$) and characterise the behaviour of the device comparing the dynamical response of narrow gap case with that of the wide gap design. We define an

Table 1
Data utilised for creating graphics.

Quantity	Value
η_{eff}	$3.3 \times 10^{-7}\,\text{N s m}^{-2}$
η	$1.8 \times 10^{-5}\,\text{N s m}^{-2}$
W	0.45 mm
L	6 mm
d	1 μm
E	$7.81 \times 10^{10}\,\text{N m}^{-2}$
ρ_q	$2650\,\text{kg m}^{-3}$
$\mathscr{V}$	5 V

additional parameter $\upsilon = |\tilde{U}_z/\tilde{U}_x|$ which is simply the ratio between the amplitude of the sense motion and the amplitude of the drive motion. Table 1 shows the data utilised in the analysis.

4.1. Air damping influence

In the case of narrow gap design the air damping of the drive motion is significantly different from that of the sense motion: The ratio between the damping coefficients of the two motions, indeed, is given by $\zeta_z/\zeta_x = \zeta^2 = (W/d)^2$ with ζ generally higher than 100. In the wide gap design, instead, $\zeta_z/\zeta_x \approx 1$ and it is exactly 1 for a square cross section, i.e. when $\mu = 1$. The large difference between ζ_z and ζ_x in the narrow gap case strongly reduces the amplitude of the sense motion [8], so that at a first sight the wide gap design should be preferred. However, as we will show in Sections 4.4 and 4.5, the wide gap design cannot be utilised for values of μ very close to 1, since when $\mu = 1$ the range of linearity and the bandwidth of the instrument are strongly reduced. As a consequence, the only reason for choosing the wide gap design, i.e. that of having $\mu = 1$, cannot actually be utilised, thus making the narrow gap design much more interesting.

The performances of narrow gap design, indeed, can be chosen and improved by properly adjusting the additional 'free' parameter ζ. As shown in Fig. 4, the influence of ζ on the drive motion is almost absent. The parameter ζ significantly influences only the sense motion as shown in Fig. 5, where the ratio $\upsilon = |\tilde{U}_z/\tilde{U}_x|$ is represented as a function of ρ_1 for different values of ζ. It is interesting to observe that, since the narrow gap design is always characterised by $\upsilon \ll 1$, the x-component of the Coriolis force can be neglected in comparison to its z-component. The same conclusion is not always true in the case of wide gap design, as we will show in Section 4.4.

4.2. Aspect ratio influence

Fig. 6a shows the amplitude $|\tilde{U}_x(1)|$ as a function of ζ, for $\rho_1 = 1$ and different values of μ ($\mu = 0.9, 1, 1.1$). It is shown that, when a rectangular shape design is considered, it is better to choose $\mu > 1$ instead of $\mu < 1$ since in the former case the amplitude $|\tilde{U}_x(1)|$ of the free end of the beam is a bit larger. Observe that this effect is felt more for high values of ζ, because in these cases the variations of the damping coefficient $\Gamma\zeta/(\mu\rho_1 k_1)$ produced by μ are more significant.

The u_z-amplitude behaviour is analysed, for the same values of $\rho_1 = 1$ and $\mu = 0.9, 1, 1.1$, in Fig. 6b, which shows that for small ζ values, $|\tilde{U}_z(1)|$, as expected, strongly increases when $\mu = 1$, due to the matching of resonant frequencies. However, what is more important is that an increase of the parameter ζ determines a reduction of the amplitude $|\tilde{U}_z(1)|$ which is much higher for a square cross section ($\mu = 1$) than for $\mu \neq 1$, e.g. for $\mu = 0.9$ or 1.1. Observe also, that at large ζ (say $\zeta > 350$) choosing $\mu = 1.1$ gives better results than $\mu = 1$, so that a perfect square cross section cannot always guarantee a better performance.

Fig. 7 compares the behaviour of the wide and narrow gap instrument configurations. The narrow gap solution shows a smoother behaviour in the immediate surrounds of $\mu = 1$, if compared to the wide gap configuration, which in turn shows the amplitude of the sense motion depending very sharply on μ values (see Fig. 7a). Since, manufacturing errors are always present, a perfect square cross section is impossible to obtain,

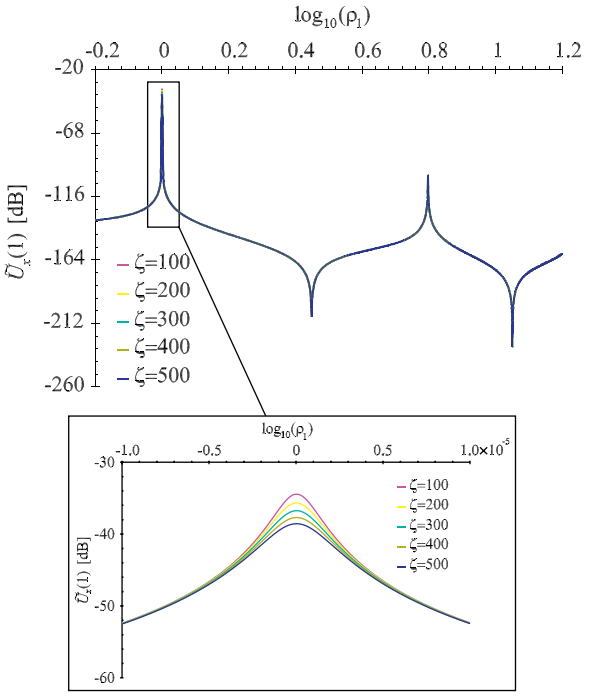

Fig. 4. Narrow gap design: the amplitude–frequency relationship for lateral vibration, with $\tilde{y}=1$, $\mu=1$, $\Omega=1\,\mathrm{rad\,s^{-1}}$, considering the secondary peaks and only the first one: it is evident the small influence of ζ.

and this will correspond to a strong signal drop (e.g. one has $|\tilde{U}_z(1)|=-63\,\mathrm{dB}$ if $\mu=1$ that becomes $|\tilde{U}_z(1)|=-91.2\,\mathrm{dB}$ for $\mu=1.001$) meaning that the potential advantage of the wide gap configuration, i.e. very small damping and, therefore, very large amplitude of the sense motion, cannot actually be obtained.

4.3. Structural damping

Structural damping is often neglected when studying these kind of devices, since it is generally negligible in comparison to the air damping. However, when the air pressure is low enough the two sources of energy dissipation may be similar and hence the structural damping has to be taken into account. This, as already briefly discussed before, is the case of a tuning fork microgyroscope in a narrow gap configuration. To be more precise, the structural damping has to be taken into account when studying the drive motion of the beam since in this case the air damping (which is related to the parameter ζ) is very small, but can be neglected when investigating the sense motion since in this case the damping factor is ζ^2 times higher. As an example, given $\rho_1=1$, $\mu=1$ and $\zeta=300$, one obtains that the air damping term in the sense motion case is $\zeta_z\Gamma/(\mu\rho_1 k_1)=0.24$, much greater than the structural term $\mu^2\eta_s/(\rho_1 k_1)^2=4.04\times10^{-7}$. On the other hand, for the drive motion, one has $\zeta_x\Gamma/(\mu\rho_1 k_1)=2.67\times10^{-6}$ and $\eta_s/(\rho_1 k_1)^2=4.04\times10^{-7}$ that are here comparable. In the case of wide gap design similar arguments show that the structural damping has to be included in the equations both for the drive and the sense motion.

4.4. Rotation rate influence

In this section we discuss the influence of the rotation rate value Ω on the instrument response.

Fig. 8 shows the quantity $|\tilde{U}_z(1)|$ as a function of Ω, for different values of ζ and μ and for the two different configurations of the instrument (wide gap and narrow gap designs). In the wide gap design, as shown in Figs. 8a and b, the only geometrical parameter that may influence the relation between $|u_z|$ and Ω is μ. Fig. 8b clearly shows that when $\mu=1$, because of a very high coupling effect, the range of linearity of the instrument is

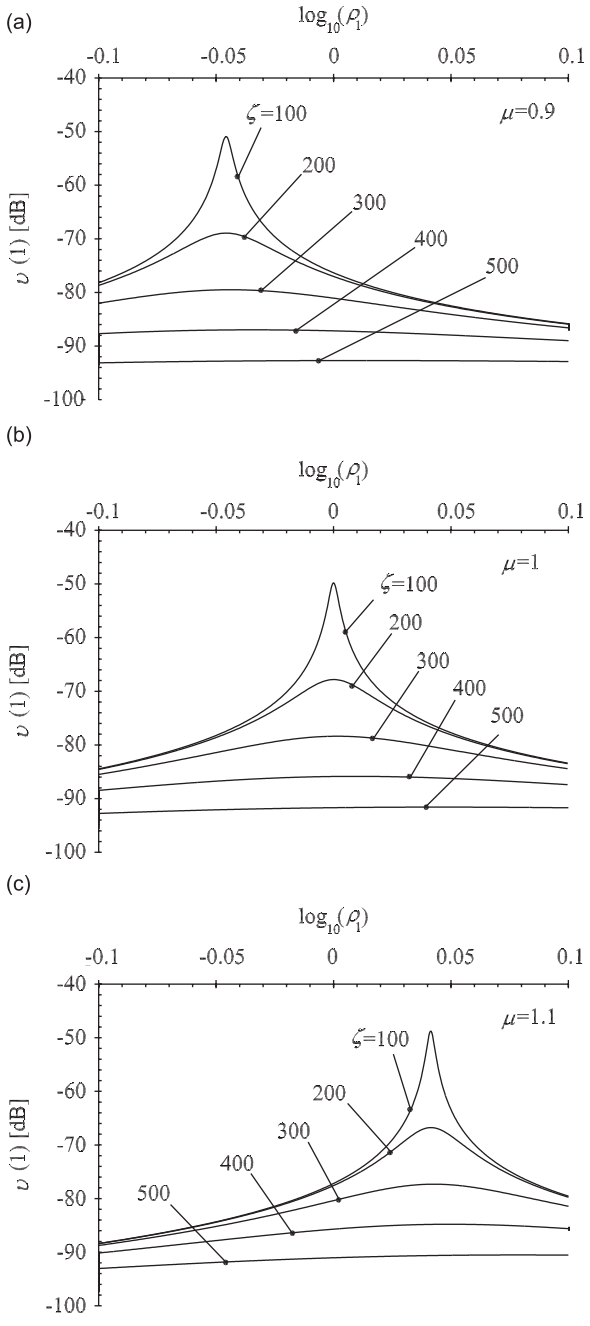

Fig. 5. Narrow gap design: the $\upsilon(1)$–frequency relationship, with $\tilde{y} = 1$, $\Omega = 1\,\mathrm{rad\,s^{-1}}$, for $\mu = 0.9$ (a), $\mu = 1$ (b) and $\mu = 1.1$ (c).

strongly reduced with respect to what is observed for $\mu = 0.9$ or 1.1 (Fig. 8a), and even more if compared to the narrow gap design (Figs. 8c and d). The very limited range of linearity of the wide gap design at $\mu = 1$ is one of the main reasons to avoid the square cross section in practical applications.

The case of the narrow gap design is instead different. Figs. 8c and d show indeed that by properly choosing the free parameter ζ it is possible to adjust the range of linearity of the instrument. In particular, if the aim of the instrument is to measure high rotation rates then ζ has to be increased. If high precision at low rotation rates is, instead, important, ζ has to be lowered to achieve the needed improvement of the instrument sensitivity $|u_z|/\Omega$.

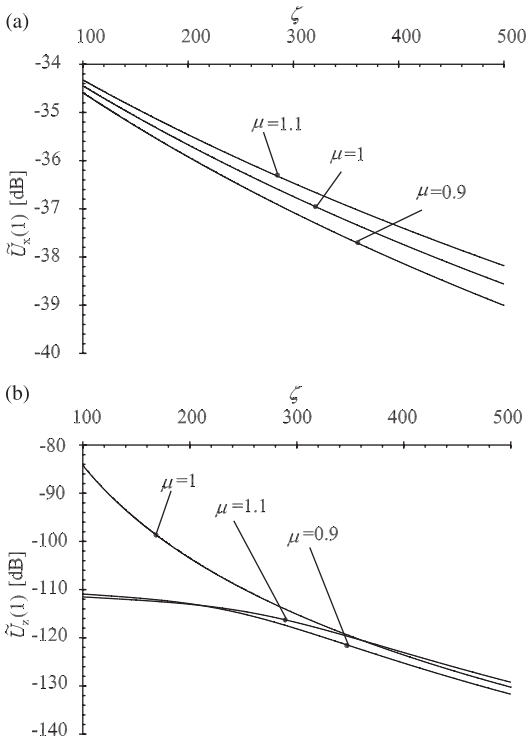

Fig. 6. Narrow gap design: the amplitude–ζ relationship for lateral vibration (a) and for vertical vibration (b), with $\tilde{y} = 1$, $\rho_1 = 1$, $\Omega = 1\,\mathrm{rad\,s^{-1}}$, for different values of μ.

4.5. The bandwidth–μ relationship

Here we describe the sensor bandwidth (BW) dependence on the mode coupling (i.e. on the beam aspect ratio μ), either in the case of constant angular rotation rate Ω_0 of the instrument (in this case the bandwidth will be referred to with the symbol BW_{Ω_0}) or when the rotation rate $\Omega(t)$ to be measured is time-dependent ($BW_{\Omega(t)}$). Both the wide and narrow gap designs will be analysed. The bandwidth BW_{Ω_0} is simply defined as the difference between the upper and lower frequencies f_B and f_A located on the two opposite sides of the resonant peak, where a 3 dB drop of the sense response amplitude occurs. The latter $BW_{\Omega(t)}$ is, instead, evaluated considering the system response to the generic excitation $\Omega(t) = \Omega_0 \cos(2\pi f_{\mathrm{rot}} t)$, and represents the maximum extension of the frequency range in which f_{rot} must be contained in order to avoid a change $\Delta\tilde{U}_z(\tilde{y}, f_{\mathrm{rot}})$ of the amplitude (the so called dynamic error) greater than ± 3 dB [28]. The derivation of the mathematical expressions of the two different bandwidths is reported in Appendix A.

Fig. 9 shows the BW_{Ω_0} vs. μ relations for the wide gap design (Fig. 9a) and for the narrow gap one (Fig. 9b). The particular non-monotonic behaviour of BW_{Ω_0} can be explained by first observing that, in a system with two close modes of vibration, the bandwidth around one of the two peaks is affected by the relative position of the two natural frequencies, and this influence is stronger if the two peak amplitudes are of the same order of magnitude. This indeed may cause the behaviour observed in Fig. 9a where as μ approaches 1 from the left or from the right, a step variation in the quantity $BW_{\Omega_0}(\mu)$ is observed. The reason of this peculiar behaviour is explained in what follows. For each given value of μ, BW_{Ω_0} is the amplitude of the frequency range in which the condition $\mathscr{M}_z \geqslant \frac{1}{2}\mathscr{M}_z|_{\max}$ is verified, where $\mathscr{M}_z$ is the mechanical energy of the system. Between the two resonant peaks, the mechanical energy $\mathscr{M}_z$ has, of course, a minimum $\mathscr{M}_z|_{\min}$. If the energy minimum $\mathscr{M}_z|_{\min}$ is greater than $\frac{1}{2}\mathscr{M}_z|_{\max}$, there is no frequency value between the two resonant peaks at which a drop of 3 dB in the amplitude response of the system can occur. In this case the range of frequencies corresponding to the bandwidth BW_{Ω_0} must contain both the resonant peaks. This happens of course for μ close enough to 1. As μ moves far from the unit value the two frequency peaks will progressively move far from each other and the

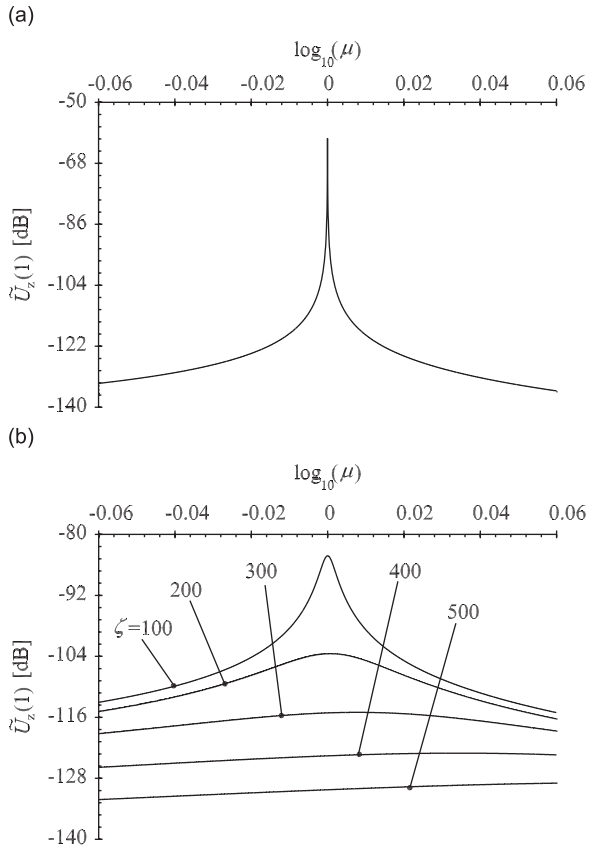

Fig. 7. The amplitude–μ relationship for vertical vibration in the wide gap design (a) and in the narrow gap one (b), with $\tilde{y}=1$, $\rho_1=1$, $\Omega=1\,\mathrm{rad\,s^{-1}}$.

mechanical energy minimum $\mathscr{M}_z|_{\min}$ will slowly decrease toward the value $\frac{1}{2}\mathscr{M}_z|_{\max}$. The resulting bandwidth BW_{Ω_0} will still contain the two resonant peaks but will slowly increase because of the increased distance between the peaks. However, as the quantity μ moves further and further from 1, at a certain value of μ the $\mathscr{M}_z|_{\min}$ will reach the value $\frac{1}{2}\mathscr{M}_z|_{\max}$. When this happens the frequency range corresponding to the bandwidth BW_{Ω_0} will now contain only one resonant peak and therefore will undergo a step reduction as shown by the dashed vertical lines in Fig. 9a. The figure also shows that for μ very close to 1, the $BW_{\Omega_0}(\mu)$ function has a minimum which is a consequence of the enhanced sharpness of the amplitude vs. frequency curve, caused by the superposition of the two resonant peaks.

Fig. 9b shows what happens when the instrument configuration is that of the narrow gap design. In this case $|u_x|_{\max}\gg|u_z|_{\max}$ as the squeeze motion is strongly damped, thus the system behaves as if it were only one resonant peak. What is important to observe is that the bandwidth increases with ζ and decreases with μ. This is related to the influence of the two parameters ζ and μ on the damping coefficient $\zeta^3\Gamma/(\mu\rho_1 k_1)$ of the sense motion. When ζ increases or μ decreases, indeed, the u_z-amplitude vs. frequency curve becomes less sharp and hence BW_{Ω_0} increases.

Figs. 10 and 11 show, respectively, the bandwidth $BW_{\Omega(t)}$ vs. μ relationship and the dynamic error evaluated at the beam end $\Delta\bar{U}_z(1,f_{\mathrm{rot}})$ as a function of f_{rot}. The wide gap design is represented by a dashed line, whereas the narrow gap case is represented, for different values of ζ, by the continuous lines. The figures show that the bandwidth $BW_{\Omega(t)}(\mu)$ always has a minimum $BW_{\Omega(t)}|_{\min}$ for values of the aspect ratio μ which are very close to 1 (both for the wide and narrow gap configurations). The case of the wide gap design, in a narrow band around $\mu=1$, is reported in the inset of Fig. 10, which shows how small $BW_{\Omega(t)}$ becomes in these conditions.

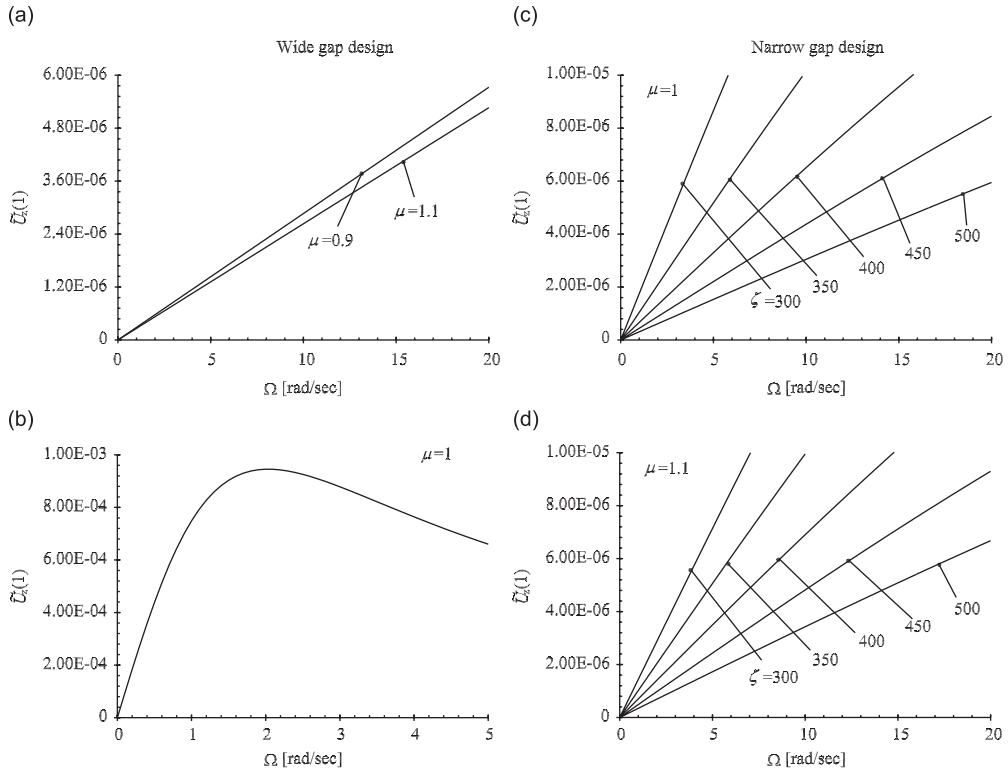

Fig. 8. The amplitude–Ω relationship for vertical vibration with $\tilde{y} = 1$, $\rho_1 = 1$, in the wide gap design for $\mu = 0.9$, $\mu = 1.1$ (a), $\mu = 1$ (b), and in the narrow gap one for $\mu = 1$ (c) and $\mu = 1.1$ (d).

This again explains why it is not convenient to use a square cross section with this kind of instrument configuration.

For ζ-values greater than 100, the narrow gap design has instead a much better behaviour in comparison to the wide gap case already at $\mu \approx 1$. The behaviour is further improved as ζ is increased whatever is the value of μ.

Fig. 11 shows the dynamic error $\Delta\bar{U}_z$ as a function of the frequency f_{rot} and for different values of the parameters μ and ζ for both the wide gap and narrow gap designs. Observe that for $\mu = 1$, as shown in Fig. 11a the dynamic error is always negative and always decreases as f_{rot} is increased. The inset in the figure shows the behaviour of the wide gap design. This configuration is characterised by a very fast decrease of the dynamic error from zero to values smaller than -3 dB thus leading to a very small bandwidth $BW_{\Omega(t)}$, as already anticipated by Fig. 10. If one changes the value of μ to, e.g. $\mu = 1.1$, as shown in Fig. 11b, the dynamic error instead is positive and increases with f_{rot}. This time a slower increase of the dynamic error from zero is observed for both the device configurations (wide and narrow gap). However, one immediately notices that only in the case of the narrow gap design, the dynamic error can be strongly reduced, for any given desired value of the bandwidth $BW_{\Omega(t)}$, by means of an appropriate choice of the parameter ζ, which however cannot be exaggeratedly increased, in order to avoid an excessive reduction of the signal response amplitude. As an example, given $BW_{\Omega(t)} \approx 600$ Hz, one could choose $\mu = 1.1$ and $\zeta = 300$, or, to have a less damped design solution, $\zeta = 250$ with $\mu = 1.06$ (Fig. 11c).

The possibility of adjusting ζ represents the main advantage of the narrow gap configuration in comparison to the wide gap solution.

5. Conclusions

In this work we have developed an accurate analytical model to describe the dynamics of a double tuning fork quartz structure microgyroscope. Two designs of the sensor have been considered, different from each

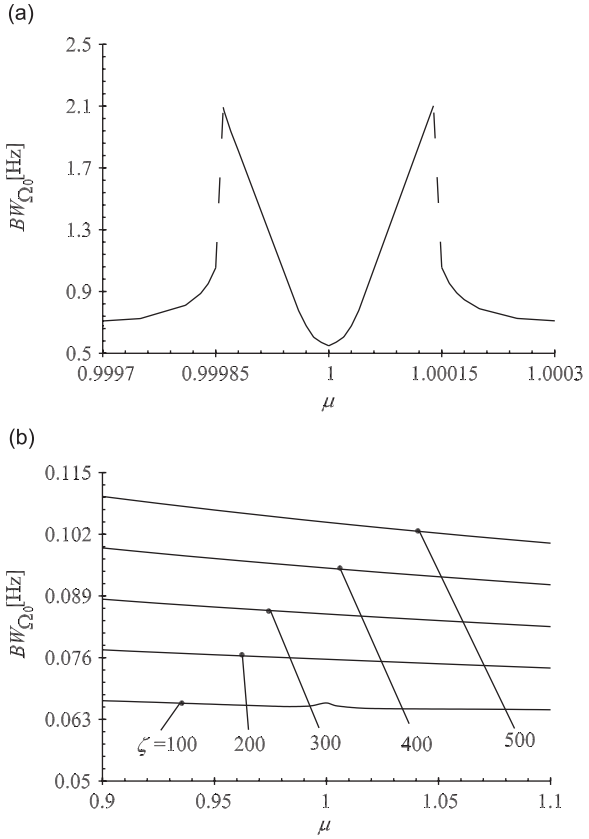

Fig. 9. $BW_{\Omega_0}-\mu$ (stationary angular rate case) relationship for the wide gap design (a) and for the narrow gap one (b), with $\tilde{y}=1$, $\rho_1=1$, $\Omega_0=1\,\mathrm{rads}^{-1}$.

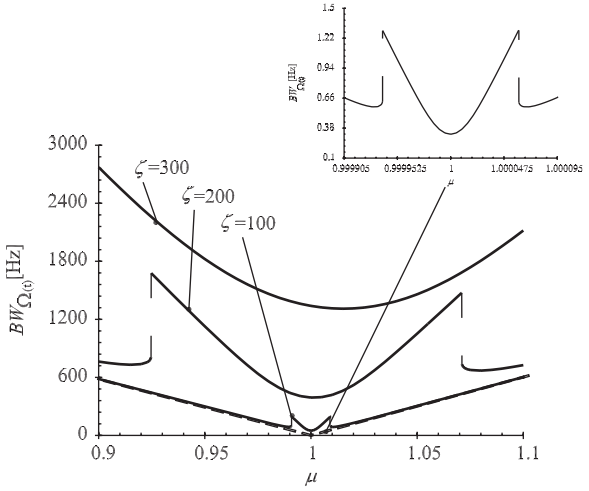

Fig. 10. $BW_{\Omega(t)}-\mu$ (harmonic rotation case) relationship for the wide gap design (dashed line) and for the narrow gap one (continuous lines), with $\tilde{y}=1$, $\rho_1=1$, $\Omega_0=1\,\mathrm{rad\,s}^{-1}$.

other for the measure of the gap between the forks and the substrate. In the former case, the 'wide gap' design, the instrument operates at atmospheric pressure and since the gap is large enough, the presence of the substrate can be neglected on the evaluation of the drag force due to air viscosity. In the latter case, the

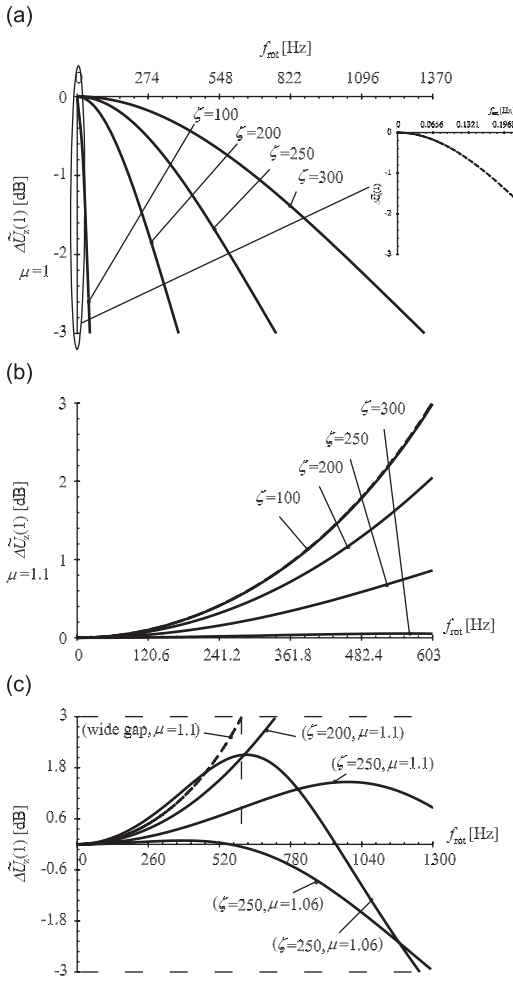

Fig. 11. $\Delta\bar{U}_z$–f_{rot} relationship, for $\mu = 1$ (a), $\mu = 1.1$ (b) and for different values of ζ and μ (c), for both the wide gap design (dashed lines) and the narrow gap one (continuous lines), with $\bar{y} = 1$, $\rho_1 = 1$, $\Omega_0 = 1\,\mathrm{rad\,s^{-1}}$.

'narrow gap' design, one has a really narrow structure–substrate gap and, hence, since the air damping is strongly influenced by the height of the gap, the device has to run vacuum-packed to have the output of the instrument strong enough. In this last case, the viscous damping in the drive (lateral) motion is very different from that in the sense (squeeze) motion, and this difference is largely affected by the additional geometrical parameter ζ, which is the ratio between the width of the beam and height of the air gap.

In the wide gap design the air damping is almost the same along both the directions and has been modelled by adapting to our case the Landau's solution for a harmonically vibrating sphere. In both the cases we have also taken into account the influence of the structural damping, which has been shown to be rather negligible, except when the air damping coefficient is very small.

Since the device is supposed to be symmetric, we have studied the behaviour of one of the two beams of the drive mode, and described it as a 1D continuum elastic body. The mathematical model has been written in a unified form, which holds for both the designs considered, making possible to compare their performances. We find out that the narrow gap design is much better than the other one because of the additional design parameter ζ, which allows the designer to (i) lower the dynamic error of the instrument, once the bandwidth is given and (ii) modify the range of the rotating rate where the response of the instrument is linear.

In particular, once the needed amplitude of the sense signal is obtained by choosing the correct air pressure value, one can regulate ζ to modify the dynamic error of the instrument in a certain bandwidth. Also the

designer has the possibility of adjusting the sensitivity of the instrument by still properly choosing ζ, e.g. if high rotation rates have to be measured, high ζ-values have to be chosen, whilst if high precision at low rotation rates is needed, lower damping, i.e. smaller values of ζ, will produce an improvement of the sensitivity.

Acknowledgement

The authors thank Prof. Luigi Mangialardi for his always useful discussions and interesting suggestions.

Appendix A. The system bandwidth

A.1. The bandwidth in the case of stationary rotation

When the gyroscope has to work at constant angular rate $\Omega = \Omega_0$, the bandwidth is usually defined as the modulus of the difference between the lower and upper frequency points f_A and f_B close to the drive motion resonant peak, where the time-averaged mechanical energy of the sense motion assumes the half value of the maximum observed in resonant condition, hence, where there is a 3 dB drop of the sense response amplitude. With the quantities defined above, we have that $BW_{\Omega_0} = |f_A - f_B| = |\rho_A - \rho_B|\omega_{n,1}^{(x)}/2\pi$ Hz. The importance of this bandwidth evaluation is related to the difficulty of achieving a perfect matching between the excitation frequency and the natural frequency of the drive motion. The possible reasons can be small deviations of the natural frequency produced by imperfections coming from the fabrication process, temperature fluctuations or errors related to the control strategy of the actuation. Hence, it is necessary to know the limits of the frequency fluctuations that produce a decrease of the output motion amplitude still utilisable for the angular rate evaluation. In the results (Section 4.5) it has been shown the trend of this kind of system bandwidth, as the modes become closer (i.e. the $BW_{\Omega_0} - \mu$ relation).

A.2. The bandwidth in the case of harmonic rotation

If the input angular rate is time dependent, the dynamic behaviour of the gyroscope is different. In particular, there is only a limited range of frequencies, again often referred to as 'bandwidth', in which the sensor is able to measure the amplitudes of the corresponding harmonics within an acceptable small error, usually referred to as 'dynamic error' or 'amplitude error' in the technical literature. To evaluate this type of bandwidth, the system response to the generic harmonic $\Omega(t) = \Omega_0 \cos(2\pi f_{\mathrm{rot}} t)$ has to be calculated. The Coriolis term of the output motion equation (22) is in this case

$$2\frac{\Omega \partial \tilde{u}_x}{\omega \, \partial \tau} = \mathrm{i}\frac{\Omega_0}{\omega}\tilde{U}_x(\tilde{y})[\mathrm{e}^{\mathrm{i}(1-\rho_{\mathrm{rot}}/\rho_1)\tau} + \mathrm{e}^{\mathrm{i}(1+\rho_{\mathrm{rot}}/\rho_1)\tau}] \tag{A.1}$$

where $\rho_{\mathrm{rot}} = 2\pi f_{\mathrm{rot}}/\omega_{n,1}^{(x)}$. It is possible to show that [29] multiplying the system response $\tilde{u}_z(\tilde{y}, \tau, \rho_{\mathrm{rot}})$ by a carrier that has known phase and frequency $\omega = \omega_{n,1}^{(x)}$ and removing the high frequency components, by filtering after the demodulation, the output is

$$\bar{u}_z(\tilde{y}, \tau, \rho_{\mathrm{rot}}) = \bar{U}_z(\tilde{y}, \rho_{\mathrm{rot}}) \cos(\rho_{\mathrm{rot}}\tau + \phi) \tag{A.2}$$

where $\bar{U}_z(\tilde{y}, \rho_{\mathrm{rot}}) = (|\tilde{U}_z^{(-)}(\tilde{y}, \rho_{\mathrm{rot}})| + |\tilde{U}_z^{(+)}(\tilde{y}, \rho_{\mathrm{rot}})|)/2$, being $|\tilde{U}_z^{(\mp)}(\tilde{y}, \rho_{\mathrm{rot}})|$ the amplitudes of the responses $\tilde{u}_z^{(\mp)}(\tilde{y}, \tau, \rho_{\mathrm{rot}})$ to the two parts of the whole Coriolis term (A.1).

It is now possible to define the absolute dynamic error due to the harmonic angular rate as

$$\Delta\bar{U}_z(\tilde{y}, \rho_{\mathrm{rot}}) = \bar{U}_z(\tilde{y}, \rho_{\mathrm{rot}}) - \bar{U}_z(\tilde{y}, 0) \tag{A.3}$$

where $\bar{U}_z(\tilde{y}, 0) = \bar{U}_z(\tilde{y}, \rho_{\mathrm{rot}} = 0)$. Hence the bandwidth $BW_{\Omega(t)}$ is the range in which the angular rate frequency can change giving rise to an amplitude error $\Delta\bar{U}_z(\tilde{y}, \rho_{\mathrm{rot}})$ smaller than ± 3 dB.

Appendix B. Analytical solutions of the governing equations

B.1. Coupled system solution

In this section two different approaches to the analytical solution of the homogeneous system of partial differential equations (21) and (22) are presented. If the x-component of the distributed Coriolis force is not neglected, in both the wide gap and narrow gap cases, we obtain the following coupled system of the unknown complex functions $\tilde{u}_x(\tilde{y},\tau)$ and $\tilde{u}_z(\tilde{y},\tau)$

$$\frac{\partial^2\tilde{u}_x}{\partial\tau^2}+\zeta_x\frac{\Gamma}{\mu\rho_1 k_1}\frac{1}{\partial\tau}\frac{\partial\tilde{u}_x}{\partial\tau}+2\frac{\Omega\partial\tilde{u}_z}{\omega\,\partial\tau}+\frac{1+\mathrm{i}\eta_s\partial^4\tilde{u}_x}{\rho_1^2k_1^2}\frac{}{\partial\tilde{y}^4}=0 \tag{B.1}$$

$$\frac{\partial^2\tilde{u}_z}{\partial\tau^2}+\zeta_z\frac{\Gamma}{\mu\rho_1 k_1}\frac{1}{\partial\tau}\frac{\partial\tilde{u}_z}{\partial\tau}-2\frac{\Omega\partial\tilde{u}_x}{\omega\,\partial\tau}+\frac{1+\mathrm{i}\eta_s}{\rho_1^2k_1^2}\mu^2\frac{\partial^4\tilde{u}_z}{\partial\tilde{y}^4}=0 \tag{B.2}$$

Let $\tilde{\mathbf{u}}(\tilde{y},\tau)=\{\tilde{u}_x(\tilde{y},\tau),\tilde{u}_z(\tilde{y},\tau)\}^{\mathrm{T}}$. The system can be conveniently rephrased in matrix notation as

$$\mathbf{I}_2\tilde{\mathbf{u}}_{\tau\tau}+\tilde{\mathbf{C}}\tilde{\mathbf{u}}_{\tau}+\tilde{\mathbf{K}}\tilde{\mathbf{u}}_{\tilde{y}\tilde{y}\tilde{y}\tilde{y}}=\mathbf{0} \tag{B.3}$$

where

$$\tilde{\mathbf{C}}=\begin{bmatrix}\zeta_x\dfrac{\Gamma}{\mu\rho_1k_1}\dfrac{1}{} & 2\dfrac{\Omega}{\omega}\\ -2\dfrac{\Omega}{\omega} & \zeta_z\dfrac{\Gamma}{\mu\rho_1k_1}\dfrac{1}{}\end{bmatrix},\quad \tilde{\mathbf{K}}=\frac{1+\mathrm{i}\eta_s}{\rho_1^2k_1^2}\begin{bmatrix}1 & 0\\ 0 & \mu^2\end{bmatrix}$$

and $\mathbf{I}_2$ is the second-order identity matrix.

The system has to be solved by taking into account a proper set of boundary conditions. In the cantilever beam case, they are $\tilde{\mathbf{u}}(0,\tau)=0,\partial\tilde{\mathbf{u}}(0,\tau)/\partial\tilde{y}=0$, $\partial^2\tilde{\mathbf{u}}(1,\tau)/\partial\tilde{y}^2=\{\mathscr{A}_{\mathrm{piezo}}L\,\mathrm{e}^{\mathrm{i}\tau},0\}^{\mathrm{T}}$, $\partial^3\tilde{\mathbf{u}}(1,\tau)/\partial\tilde{y}^3=0$.

Since the searched solution is the steady bending motion, in two planes, of a forced vibrating beam, with excitation frequency equal to ω, no initial conditions are needed and a general solution of the form $\tilde{\mathbf{U}}\,\mathrm{e}^{\mathrm{i}(\tau-kL\tilde{y})}$ has to be considered, where k is the complex wavenumber. By substituting this kind of solution in the system, one gets

$$(-\mathbf{I}_2+\mathrm{i}\tilde{\mathbf{C}}+\tilde{k}^4\tilde{\mathbf{K}})\tilde{\mathbf{U}}=\mathbf{0} \tag{B.4}$$

where $\tilde{k}=kL$. Multiplying the whole equation by $\tilde{\mathbf{K}}^{-1}$, one obtains the following eigenvalue problem

$$[\tilde{\mathbf{K}}^{-1}(\mathbf{I}_2-\mathrm{i}\tilde{\mathbf{C}})-\tilde{k}^4\mathbf{I}_2]\tilde{\mathbf{U}}=\mathbf{0} \tag{B.5}$$

Let $(\tilde{k}^4)_i$ and $\mathbf{\Psi}_i$, with $i=1,2$, be the eigenvalues and the corresponding eigenvectors and k_{ij}, with $j=1,4$, the four complex roots of the i-th eigenvalue. The solution can be written as

$$\tilde{\mathbf{u}}(\tilde{y},\tau)=\sum_{i=1}^{2}\mathbf{\Psi}_i\sum_{j=1}^{4}U_{ij}\,\mathrm{e}^{\mathrm{i}(\tau-\tilde{k}_{ij}\tilde{y})} \tag{B.6}$$

where the complex constants U_{ij} have to be evaluated by taking into account the boundary conditions.

B.2. Uncoupled system solution

If the x-component of the distributed Coriolis force is considered negligible, one is able to solve the two equations of the system independently one from the other. The first to be solved is, of course, the drive motion homogeneous PDE

$$\frac{\partial^2\tilde{u}_x}{\partial\tau^2}+\zeta_x\frac{\Gamma}{\mu\rho_1k_1}\frac{1}{\partial\tau}\frac{\partial\tilde{u}_x}{\partial\tau}+\frac{1+\mathrm{i}\eta_s\partial^4\tilde{u}_x}{\rho_1^2k_1^2}\frac{}{\partial\tilde{y}^4}=0 \tag{B.7}$$

Moving from a general solution of the form $\tilde{U}_x e^{i(\tau-\tilde{k}_x\tilde{y})}$, with the same meaning of symbols involved, one gets

$$\tilde{k}_x^4 = \frac{\rho_1^2 k_1^2}{1+i\eta_s}\left(1 - i\zeta_x \frac{\Gamma}{\mu\rho_1 k_1}\right) \tag{B.8}$$

and the solution can be written as

$$\tilde{u}_x(\tilde{y},\tau) = \sum_{j=1}^{4} \tilde{U}_{xj} e^{i(\tau-\tilde{k}_{xj}\tilde{y})} \tag{B.9}$$

where the complex constants $\tilde{U}_{xj}$ have to be evaluated by the boundary conditions: $\tilde{u}_x(0,\tau)=0$, $\partial\tilde{u}_x(0,\tau)/\partial\tilde{y}=0$, $\partial^2\tilde{u}_x(1,\tau)/\partial\tilde{y}^2 = \mathscr{A}_{\text{piezo}} L e^{i\tau}$, $\partial^3\tilde{u}_x(1,\tau)/\partial\tilde{y}^3=0$.

The sense motion equation can now be written as

$$\frac{\partial^2\tilde{u}_z}{\partial\tau^2} + \zeta_z\frac{\Gamma}{\mu\rho_1 k_1}\frac{\partial\tilde{u}_z}{\partial\tau} + \mu^2\frac{1+i\eta_s\partial^4\tilde{u}_z}{\rho_1^2 k_1^2 \partial\tilde{y}^4} = i2\frac{\Omega}{\omega}\sum_{j=1}^{4}\tilde{U}_{xj}e^{i(\tau-\tilde{k}_{xj}\tilde{y})} \tag{B.10}$$

with a known term at the RHS. The general solution is $\tilde{u}_z(\tilde{y},\tau) = \tilde{u}_z^{(o)}(\tilde{y},\tau) + \tilde{u}_z^{(p)}(\tilde{y},\tau)$, sum of the solution $\tilde{u}_z^{(o)}(\tilde{y},\tau)$ of the associated homogeneous equation and of a particular integral $\tilde{u}_z^{(p)}(\tilde{y},\tau)$ of the entire equation. Regarding this last term, since it has to be of the same form of the known term, it is possible to show that

$$\frac{\tilde{U}_{zj}^{(p)}}{\tilde{U}_{xj}} = \frac{i2\dfrac{\Omega L^2}{cr_z}}{\rho_1 k_1(\mu^2-1) - i\dfrac{\Gamma}{\mu}\zeta_z\left(\mu^2\dfrac{\zeta_x}{\zeta_z}-1\right)} = \mathscr{S} \tag{B.11}$$

and, hence

$$\tilde{u}_z^{(p)}(\tilde{y},\tau) = \mathscr{S}\tilde{u}_x(\tilde{y},\tau) \tag{B.12}$$

It is important to stress that the structural damping coefficient η_s does not appear at all in the expression of the complex value $\mathscr{S}$.

Regarding the solution of the associated homogeneous equation $\tilde{u}_z^{(o)}(\tilde{y},\tau)$, if a solution as $\tilde{U}_z e^{i(\tau-\tilde{k}_z\tilde{y})}$ is considered, it is possible to obtain

$$\tilde{k}_z^4 = \frac{1}{\mu^2}\frac{\rho_1^2 k_1^2}{1+i\eta_s}\left(1 - i\zeta_z\frac{\Gamma}{\mu\rho_1 k_1}\right) \tag{B.13}$$

and the solution can be written as

$$\tilde{u}_z(\tilde{y},\tau) = \sum_{j=1}^{4}(\tilde{U}_{zj}e^{-i\tilde{k}_{zj}\tilde{y}} + \mathscr{S}\tilde{U}_{xj}e^{-i\tilde{k}_{xj}\tilde{y}})e^{i\tau} \tag{B.14}$$

where the complex constants $\tilde{U}_{zj}$ have to be evaluated by considering the appropriate boundary conditions. As usual, for the cantilever beam they are $\tilde{u}_z(0,\tau)=0$, $\partial\tilde{u}_z(0,\tau)/\partial\tilde{y}=0$, $\partial^2\tilde{u}_z(1,\tau)/\partial\tilde{y}^2=0$, $\partial^3\tilde{u}_z(1,\tau)/\partial\tilde{y}^3=0$.

At last a particular case of uncoupled solution has to be considered. It is the one corresponding to $\mu=1$ (i.e. square cross section) when $\zeta_x=\zeta_z$, interesting for the applications only in the case of the wide gap design. In this situation $\tilde{k}_{xj}=\tilde{k}_{zj}$ and, hence, the particular integral of the output motion is no more the one reported in Eq. (B.12), but it is of the form $\tilde{y}\tilde{U}_{zj}^{(p)}e^{i(\tau-\tilde{k}_{xj}\tilde{y})}$. One gets

$$\frac{\tilde{U}_{zj}^{(p)}}{\tilde{U}_{xj}} = \frac{\dfrac{1}{2}\dfrac{\Omega L^2}{cr_z}}{\dfrac{1+i\eta_s}{\rho_1 k_1}\tilde{k}_{xj}^3} = \mathscr{S}_j \tag{B.15}$$

and, hence

$$\tilde{u}_z(\tilde{y},\tau) = \sum_{j=1}^{4} (\tilde{U}_{zj} + \tilde{y}\mathscr{S}_j \tilde{U}_{xj})\, \mathrm{e}^{\mathrm{i}(\tau - \tilde{k}_{xj}\tilde{y})} \tag{B.16}$$

The uncoupled solution presents, hence, in this particular case, a sort of spatial resonance, since one has the coincidence of the eigenvalues of the two motions. It is important to point out that, since in the coupled solution the eigenvalues are always different in value, this phenomenon does not belong to the dynamics of coupled systems.

References

[1] Y. Mochida, M. Tamura, K. Ohwada, A micromachined vibrating rate gyroscope with independent beams for the drive and detection modes, *Sensors and Actuators* 80 (2000) 170–178.

[2] Y. Oh, B. Lee, S. Baek, H. Kim, J. Kim, S. Kang, C. Song, A tunable vibratory microgyroscope, *Sensors and Actuators A* 64 (1998) 51–56.

[3] H. Kawai, K.-I. Atsuchi, M. Tamura, K. Ohwada, High-resolution microgyroscope using vibratory motion adjustment technology, *Sensors and Actuators A* 90 (2001) 153–159.

[4] T. Tsuchiya, Y. Kageyama, H. Funabashi, J. Sakata, Vibrating gyroscope consisting of three layers of polysilicon thin films, *Sensors and Actuators* 82 (2000) 114–119.

[5] T. Tsuchiya, Y. Kageyama, H. Funabashi, J. Sakata, Polysilicon vibrating gyroscope vacuum-encapsulated in an on-chip microchamber, *Sensors and Actuators A* 90 (2001) 49–55.

[6] S.E. Alper, T. Akin, A symmetric surface micromachined gyroscope with decoupled oscillation modes, *Sensors and Actuators A* 97 (2002) 347–358.

[7] S.E. Alper, T. Akin, Symmetrical and decoupled nickel microgyroscope on insulating substrate, *Sensors and Actuators A* 115 (2004) 336–350.

[8] B. Xiong, L. Che, Y. Wang, A novel bulk micromachined gyroscope with slots structure working at atmosphere, *Sensors and Actuators A* 107 (2003) 137–145.

[9] K. Maenaka, T. Fujita, Y. Konishi, M. Maeda, Analysis of a highly sensitive silicon gyroscope with cantilever beam as vibrating mass, *Sensors and Actuators A* 54 (1996) 568–573.

[10] X. Li, M. Bao, H. Yang, S. Shen, D. Lu, A micromachined piezoresistive angular rate sensor with a composite beam structure, *Sensors and Actuators* 72 (1999) 217–223.

[11] S. Sassen, R. Voss, J. Schalk, E. Stenzel, T. Gleissner, R. Gruenberger, F. Neubauer, W. Ficker, W. Kupke, K. Bauer, M. Rose, Tuning fork silicon angular rate sensor with enhanced performance for automotive applications, *Sensors and Actuators* 83 (2000) 80–84.

[12] O. Bochobza-Degani, D.J. Seter, E. Socher, Y. Nemirovsky, A novel micromachined vibrating rate-gyroscope with optical sensing and electrostatic actuation, *Sensors and Actuators* 83 (2000) 54–60.

[13] H. Yang, B. Minhang, H. Yin, S. Shen, A novel bulk micromachined gyroscope based on a rectangular beam-mass structure, *Sensors and Actuators A* 96 (2002) 145–151.

[14] S. Rajendran, K. Liew, Design and simulation of an angular-rate vibrating microgyroscope, *Sensors and Actuators A* 116 (2004) 241–256.

[15] S.D. Senturia, *Microsystem Design*, Kluwer Academic Publishers, Dordrecht, 2004.

[16] K. Tanaka, Y. Mochida, M. Sugimoto, K. Moriya, T. Hasegawa, K. Atsuchi, K. Ohwada, A micromachined vibrating gyroscope, *Sensors and Actuators A* 50 (1995) 111–115.

[17] R. Lifshitz, M.L. Roukes, Thermoelastic damping in micro- and nanomechanical systems, *Physical Review B* 61 (8) (2000) 5600–5609.

[18] E.A. Avallone (Ed.), *Standard Handbook for Mechanical Engineers*, McGraw-Hill, New York, 1987.

[19] K. Kokubun, M. Hirata, H. Murakami, Y. Toda, M. Ono, A bending and stretching mode crystal oscillator as a friction vacuum gauge, *Vacuum* 34 (1984) 731–735.

[20] K. Kokubun, M. Hirata, M. Ono, H. Murakami, Y. Toda, Unified formula describing the impedance dependence of a quartz oscillator on gas pressure, *Journal of Vacuum Science & Technology A* 5 (4) (1987) 2450–2453.

[21] F.R. Blom, S. Bouwstra, M. Elwenspoek, J.H.J. Fluitman, Dependence of the quality factor of micromachined silicon beam resonators on pressure and geometry, *Journal of Vacuum Science & Technology B* 10 (1) (1992) 19–26.

[22] H. Hosaka, K. Itao, S. Kuroda, Damping characteristics of beam-shaped micro-oscillators, *Sensors and Actuators A* 49 (1995) 87–95.

[23] L. Landau, E. Lifshitz, *Fluid Mechanics* (*Course of Theoretical Physics*), Butterworth-Heinemann, Elsevier Science & Technology Books, Linacre House, Jordan Hill, Oxford, 2000, ISBN 0-08-033932-8.

[24] T. Veijola, H. Kuisma, J. Lahdenpera, T. Ryhanen, Equivalent-circuit model of the squeezed gas film in a silicon accelerometer, *Sensors and Actuators A* 48 (1995) 239–248.

[25] T. Veijola, T. Ryhanen, H. Kuisma, J. Lahdenpera, Circuit simulation model of gas damping in microstructures with non trivial geometries, in: *Transducers* '95—*Eurosensors* IX, Stockholm, 1995, pp. 36–39.

[26] B.J. Hamrock, *Fundamentals of Fluid Film Lubrication*, McGraw-Hill, New York, 1994.

[27] W.G. Cady, *Piezoelectricity: An Introduction to the Theory and Application of Electromechanical Phenomena in Crystal*, McGraw-Hill, New York, 1943.
[28] J. Soderkvist, Piezoelectric beams and vibrating angular rate sensors, *IEEE Transactions on Ultrasonics, Ferroelectrics, and Frequency Control* 38 (1991) 271–280.
[29] V.A. Apostolyuk, V.J. Logeeswaran, F.E.H. Tay, Efficient design of micromechanical gyroscopes, *Journal of Micromechanics and Microengineering* 12 (2002) 948–954.